Microscopic mechanisms of high-order wave mixing in solids

David N. Purschke [1,*] Álvaro Jiménez-Galán [1,2,†] Thomas Brabec,[3] Andrei Yu. Naumov,[1] André Staudte [1]
David M. Villeneuve [1] and Giulio Vampa[1]

[1]*Joint Attosecond Science Laboratory, National Research Council of Canada and University of Ottawa, Ottawa, Ontario, Canada K1A 0R6*
[2]*Max Born Institute, Berlin D-12489, Germany*
[3]*Department of Physics, University of Ottawa, Ottawa, Ontario, K1N 6N5, Canada*

The gas-phase technique of noncollinear two-color excitation is adapted to study extreme-ultraviolet high-order harmonic generation (HHG) in magnesium oxide. We observe high-order wave-mixing pathways with brightness comparable to that of the single-color HHG. Simulations reveal that the efficiencies are dominated by the microscopic physics as opposed to macroscopic effects. Building on previous work, we develop a general analytic theory of high-order wave mixing that explains our observations and demonstrates how a perturbative nonlinear optical framework emerges form the interaction between the weak field and the laser-dressed state of the crystal in the strong-field approximation. The theory outlines a photon-mixing picture of high-order wave mixing and connects the strong asymmetry between sum- and difference-frequency pathways to the cutoff in the HHG spectrum. Our work establishes the potential of high-order wave mixing as a probe of the microscopic attosecond physics in solids and points to new opportunities in solid-state strong-field photonics.

Introduction. The merging of attosecond and solid-state physics has led to new research directions in solid-state light-wave electronics, where the electric field waveform of light is used to coherently drive attosecond currents [1–3]. These currents lead to the emission of harmonic radiation, which is sensitive to the crystal properties [3–8] and can be controlled with external fields and structures [9–12]. The adaptation of gas-phase collinear two-color techniques to solids has led to fundamental insights into the nature of solid-state HHG [13–15]. In gases, employing a noncollinear geometry leads to spatially separate beams corresponding to the high-order wave-mixing pathways between the driving fields [16]. The power scaling of the different wave-mixing orders suggests that a perturbative framework can be built around strong-field optical interactions, which is the precursor to many attosecond spatiotemporal control techniques [17–20]. Several studies have focused on the role of phase matching in noncollinear HHG [21,22] and, furthermore, it was thought that even the propagation angle between the two driving fields can affect the wave-mixing amplitudes. While a complete symmetry theory was recently developed to explain the origin of the perturbative scaling [23], to date there has been no investigation of the microscopic mechanisms governing the wave-mixing efficiencies. Furthermore, the emergence of solid-state HHG also elicits new questions, such as how the band structure and dephasing affect the high-order wave mixing.

Here, we adapt the noncollinear two-color excitation technique to the solid state and use it to isolate the wave-mixing pathways of extreme ultraviolet (XUV) harmonics in

magnesium oxide (MgO). We develop a numerical framework that isolates the roles of microscopic and macroscopic effects, which shows that, in contrast to gas phase, the wave-mixing efficiencies are dominated by the microscopic physics. Furthermore, we introduce an analytic theory of two-color HHG in the strong-field approximation (SFA) that isolates expressions for the wave-mixing dipoles, revealing how they diffract, the selection rules that govern their spectra, and the origin of their perturbative scaling. The theory leads to a photon-mixing picture of high-order wave mixing, where sum- and difference-frequency generation pathways (SFG and DFG, respectively) push the spectrum upwards and downwards in energy, respectively, and connects the pronounced asymmetry between the two to the roll off in the HHG amplitude near the cutoff.

XUV high-order wave mixing in MgO. The experiment is shown schematically in Fig. 1(a). A p-polarized 800 nm pulse and its second harmonic are focused onto a single-crystal MgO (100) sample with incidence angles of 60° from normal and a separation angle, $\gamma \approx 1.5°$, between the two beams. The XUV radiation emitted from the nonperturbative HHG process is collected in a reflection geometry to avoid distortion of the driving laser field by self-phase modulation in the bulk [24]. Wave-vector conservation can be used to predict the propagation angle of the different pathways, with $\vec{k}_\Omega = n_\omega \vec{k}_\omega + n_{2\omega} \vec{k}_{2\omega}$, as seen in Fig. 1(b) [16]. Furthermore, the wave-mixing pathways can be classified as SFG or DFG depending on whether the 2ω photon is added or removed [22]. The wave vectors of SFG (DFG) beams lie between (outside) those of the driving fields. The photon energy of each pathway is $\hbar\Omega = (n_\omega + 2n_{2\omega})\hbar\omega$ and the centrosymmetry of MgO enforces the parity selection rule that an odd total number of photons contributes to each pathway, $n_\omega + n_{2\omega} = 2j + 1$ [16,25,26]. Figure 1(c) shows an image of the

*dpurschk@uottawa.ca
†Present address: Instituto de Ciencia de Materiales de Madrid, C. Sor Juana Ins de la Cruz 3, 28049 Madrid.
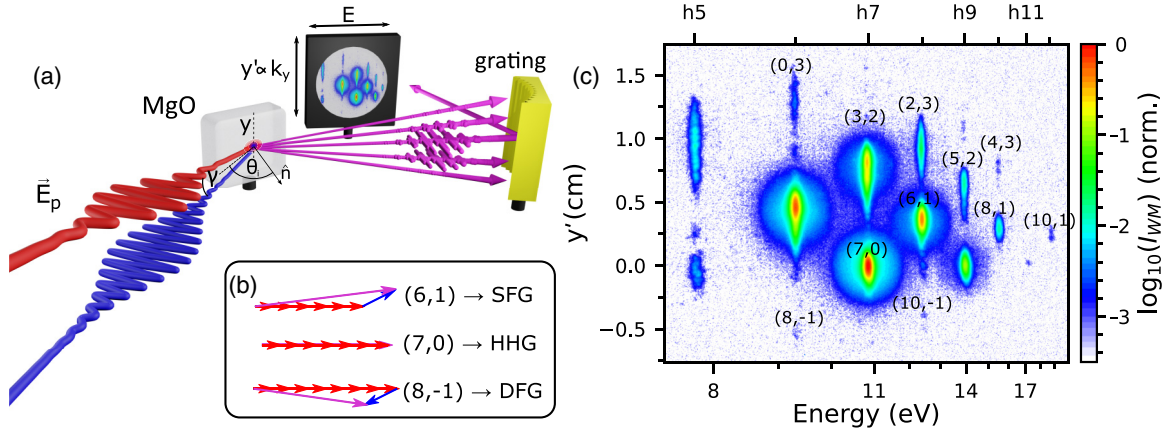
FIG. 1. (a) Schematic layout of the experimental geometry. The laser field consists of noncollinear two-color field (800 nm, 400 nm) incident on a single-crystal MgO sample. The two beams are incident upon the sample in the same vertical plane; the high-order harmonics are emitted in the specular direction in the same vertical plane. The resulting high-order harmonics are collected by an XUV spectrometer that images the source onto a microchannel plate (MCP) in the dispersion direction while allowing them to diverge in the other axis, thereby creating a map of photon energy and divergence angle. (b) Wave-vector matching diagrams with exemplary mixing processes. (c) Log-scale normalized image of the diffraction pattern on the MCP where I_{WM} is the wave-mixing intensity. Several pathways are labeled by their process orders with $(n_\omega, n_{2\omega})$.

measured high-order wave mixing with estimated intensities of $15\,\mathrm{TW/cm^2}$ and $1\,\mathrm{TW/cm^2}$ in the ω (800 nm) and 2ω (400 nm) pulses, respectively. The pathways can be systematically indexed by beginning at one of the known harmonics and moving upwards along the staircaselike structure towards the SFG pathways by removing (adding) an ω (2ω) photon [16]. Conversely, the DFG processes can be indexed by moving downwards and adding (removing) an ω (2ω) photon. The dominant structure of the diffraction pattern is governed by the odd-photon number selection rule such that odd (even)-order processes in $n_{2\omega}$ contain even (odd)-order harmonics.

In Fig. 2(a), we plot the scaling of peak intensities extracted from Gaussian fits to the experimentally measured images, revealing that the perturbative scaling observed in gas phase also holds in solid-state high-order wave mixing and strengthening the link between HHG in solids and gases [13,16]. Thus, despite operating in a nonperturbative regime, a perturbative framework emerges from the interaction between the weak field and the laser-dressed state of the crystal. Figure 2(a) also reveals that the intensities of several wave-mixing processes can even exceed that of the strongest harmonic in the single-color HHG spectrum at this ω intensity.

The wave-mixing pattern in Fig. 1(c) also reveals a pronounced asymmetry in the number and intensity of SFG versus DFG processes. Figure 3(a) shows the scaling of the two DFG processes we observe, $(10, -1)$ and $(8, -1)$, along with the SFG counterparts of the same final harmonic order (eighth and sixth, respectively). Note that this comparison is motivated by previous analytic theories of perturbed HHG, which will be expanded in a following section. In each case, the DFG intensity is more than three orders of magnitude lower than that of the SFG. Also, note that comparing wave-mixing pathways in the same order of the perturbing fields [e.g., $(8, 1)$ vs $(8, -1)$] also yields a strong asymmetry [see Fig. 1(c)].

Microscopic vs macroscopic effects. Having introduced the predominant experimental aspects of the high-order wave

mixing, we turn to modeling our observations. In the non-collinear geometry, the time delay between the fundamental field and its second harmonic varies as a function of the transverse coordinate as $\tau = y \sin(\gamma)/c$, where c is the speed of light. The relative phase between the two pulses is therefore proportional to y, i.e., $\phi \propto y$. The HHG is sensitive to the relative phase of the driving pulses [13,27], thus, the 2ω field modulates the HHG dipole, $\tilde{d}(y, \omega)$, periodically in space [17,19]. The collective behavior of the emitters determines the far-field diffraction pattern, which, in the Fresnel approximation, is calculated as [28],

$$\tilde{E}\left(\frac{y'}{\lambda z}, z, \omega\right) \propto \mathcal{F}_{y \to y'}\{\tilde{d}(y, \omega)e^{i\frac{\omega}{2cz}y^2}\}, \tag{1}$$

where z is the distance from source plane to detector plane, and y and y' are the transverse dimensions at the source and detector planes, respectively. Wave-mixing peaks in the detector plane are therefore associated with spatial harmonics of the HHG dipole in y and the wave-mixing sources are traveling waves with SFG (DFG) pathways that correspond to propagating-wave sources traveling upwards (downwards) in y. The linear relationship between y and ϕ implies that, microscopically, wave-mixing pathways are associated with harmonics of the HHG dipole in the relative phase of the two pulses, ϕ. This agrees with intuition from interferometry where the Fourier transform of time-delay scans can be used to isolate excitation pathways [29].

To calculate the HHG dipole, we solve the semiconductor Bloch equations [30–32], utilizing a two-color driving field and cosine bands with a bandwidth and gap equal to that of MgO. To elucidate the roles of microscopic and macroscopic effects [33,34], and thus quantify the effect of focal averaging and the propagation angle between the two pulses (see Supplemental Material, II [35]), we simulate the wave-mixing spectra in two ways. In the first way, the HHG dipole is calculated as a function of the 2ω carrier-envelope phase (CEP), φ, yielding $\tilde{d}(\varphi, \omega)$. The Fourier transform with
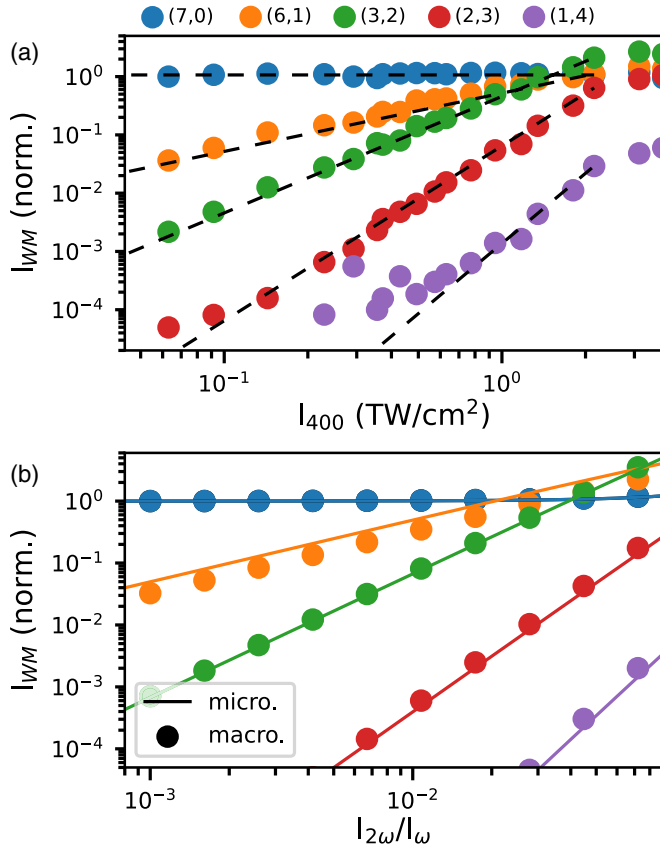
FIG. 2. (a) Measured wave-mixing intensity normalized to the (7,0) peak for several pathways as a function of 400 nm pulse intensity. The 800 nm intensity was fixed and estimated to be $17\,\mathrm{TW/cm^2}$. The black dashed lines indicate the slope expected for the power-law scaling associated with each diffraction order. (b) Calculated scaling of the microscopic (lines) and macroscopic (circles) wave-mixing intensities extracted using the CEP method and the one-dimensional (1D) grid of emitters, respectively, for the same pathways as in (a). The intensity of the ω pulse was adjusted to yield the experimental harmonic cutoff.
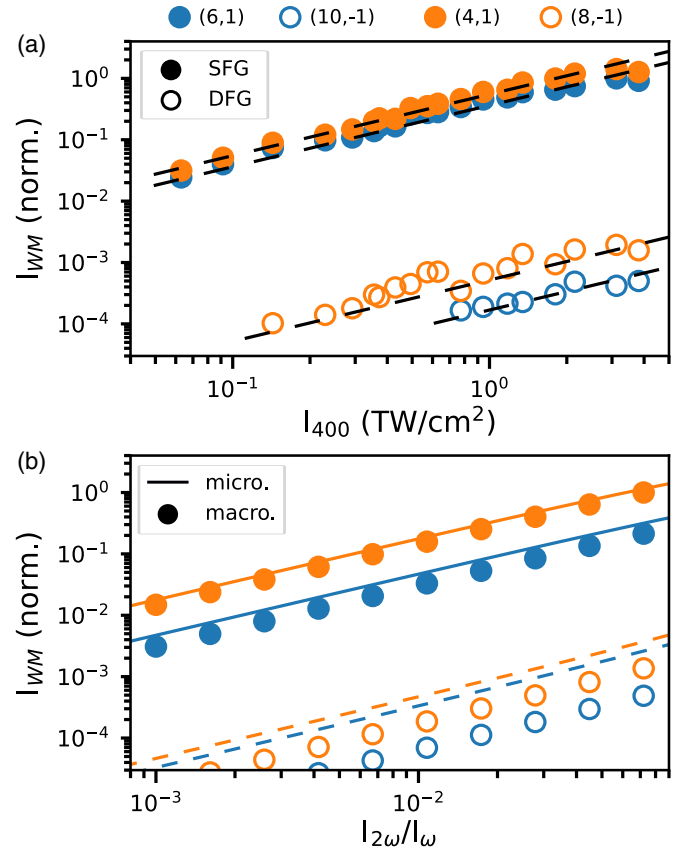
FIG. 3. (a) Comparison of experimentally measured SFG (solid circles) and DFG (open circles) wave-mixing intensities as a function of 400 nm intensity. The dashed lines are linear functions in I_{400}. (b) Microscopic (lines) and macroscopic (circles) wave-mixing intensities, calculated using the CEP method and 1D grid of emitters, respectively, as a function of the intensity ratio of the $2\omega/\omega$ pulses for the same processes as in (a). The solid (open) circles and solid (dashed) lines correspond to the SFG (DFG) pathways.

respect to φ yields the mth-order wave-mixing spectrum, $\tilde{d}(e^{im\varphi}, \omega)$, where $m = n_{2\omega}$. This method yields the microscopic, or single-emitter, spectra.

In the second way, focal averaging is introduced by calculating $\tilde{d}(y, \omega)$ on a 1D grid at the sample location with time delays and amplitudes of the driving fields taken as a function of y. We do not consider phase-matching effects because the harmonics are collected from only a subwavelength region near the surface. The far-field wave-mixing pattern is calculated using Eq. (1), yielding the collective (macroscopic) wave-mixing spectra. Note that the macroscopic spectra contain both the microscopic and macroscopic effects. The calculated wave-mixing spectra from both methods demonstrate the correct selection rules, the large SFG (DFG) asymmetry, and relative intensity of many processes (Supplemental Material, I A [35]). The model also reproduces the perturbative scaling of the wave-mixing pathways with respect to the intensity of the 2ω pulses, as shown in Fig. 2(b) for both the collective and single-emitter techniques. Notably, the latter method is significantly more

computationally efficient, which will be useful for future studies of wave mixing using *ab initio* or many-band methods [31,33,36]. The microscopic and macroscopic intensities agree within a factor of 2–3, showing that the efficiencies are dominated by the microscopic physics. Likewise, microscopic physics is predominantly responsible for the ratio of SFG and DFG processes, as seen in Fig. 3(b). The single-emitter calculations (lines) predict an SFG (DFG) ratio of over 100, with macroscopic effects (circles) contributing an additional factor of 2–3, which can be traced to focal averaging.

Wave mixing in the strong-field approximation. While the numerical solution of the semiconductor Bloch equations is a powerful approach that reproduces many aspects of our data, it does not provide an intuitive physical picture. Previous theoretical work suggested that the HHG dipole modulates with the relative phase proportionally to $\sin(\phi)$ for even-order harmonics and $\cos(\phi)$ for odd-order harmonics with an amplitude given by the single-color HHG dipole at the same harmonic order [19,27,37–39]. From Eq. (1), this predicts equal amplitude SFG and DFG. The large SFG (DFG) asymmetry at the microscopic level is therefore surprising. Here, we develop a

general theory of high-order wave mixing within the SFA that can explain the SFG (DFG) asymmetry.

The HHG dipole is given by the sum over all quantum pathways recolliding at time t (Supplemental Material, III A [35]) [30,40,41]. The amplitude of each path is given by $\exp(-iS(k,t,t') - (t-t')/T_2)$, where $S(k,t,t') = \int_{t'}^{t} d\tau \, \epsilon_g[k + A(\tau)]$ is the action accumulated along a quantum path with canonical crystal momentum k born at time t' and ending at time t, ϵ_g is the momentum-dependent band gap, and $A(\tau) = A_\omega \sin(\omega\tau) + A_{2\omega} \sin(2\omega\tau - \phi)$ is the vector potential of the driving field. T_2 is a phenomenological dephasing time.

With a weak perturbation, the action can be rewritten as $S(k,t,t') \approx S_0(k,t,t') + \cos(\phi)\sigma_s - \sin(\phi)\sigma_c$, where $\sigma_s = A_{2\omega} \int_{t'}^{t} d\tau \, v_0 \sin(2\omega\tau)$ and $\sigma_c = A_{2\omega} \int_{t'}^{t} d\tau \, v_0 \cos(2\omega\tau)$, where v_0 and S_0 are the unperturbed velocity and action, respectively (Supplemental Material, III [35]) [13,27]. The phase can be expanded in harmonics of ϕ,

$$e^{-iS(k,t,t')} \approx e^{-iS_0(k,t,t')} \sum_{m=-\infty}^{\infty} \tilde{C}_m(k,t,t') e^{im\phi}, \quad (2)$$

where we define the wave-mixing coefficients, $\tilde{C}_m(k,t,t') = \sum_{h=-\infty}^{\infty} i^{m+h} J_{m+h}(\sigma_s) J_h(\sigma_c)$ (Supplemental Material, IV A [35]), where J_ν are the Bessel functions of the first kind. The full HHG dipole is given by the sum,

$$\tilde{D}(n\omega) = \sum_{m=-\infty}^{\infty} \tilde{D}_m(n\omega), \quad (3)$$

where $D_m(n\omega)$ is the mth-order wave-mixing dipole,

$$\tilde{D}_m(n\omega) = e^{im\phi}(1 - (-1)^{m+n}) \int_0^{T/2} dt \int_{-\infty}^{\infty} dk \cdot$$
$$\times \int_{-\infty}^{t} dt' \tilde{\mathcal{D}}_0(k,t,t') \tilde{C}_m(k,t,t') e^{-in\omega t} + \text{c.c.}, \quad (4)$$

where $\tilde{\mathcal{D}}_0(k,t,t')$ is the integrand of the HHG dipole in the single-color field (Supplemental Material, V [35]).

This expression applies to both gases and centrosymmetric solids. We make no assumptions about the experimental geometry: the HHG dipole results from the quantum interference of the different pathways so that two-color HHG can be considered generally as coherent control of high-order wave mixing. Equation (4) can be used to understand three key features of high-order wave mixing. As $y \propto \phi$ in the noncollinear geometry, the factor of $e^{im\phi}$ indicates how a given order will diffract [see Eq. (1)]. Furthermore, the $[1 - (-1)^{m+n}]$ term, which arises from symmetry considerations, enforces the odd-photon number selection rule [25]. Finally, in the small-argument regime, where $J_\nu(z) \propto z^\nu$, the amplitudes of the wave-mixing coefficients scale proportionally to $A_{2\omega}^{|m|}$, and therefore perturbatively in the 2ω field (Supplemental Material, IV C [35]).

To gain further insight into the microscopic mechanisms of high-order wave mixing, we use the saddle-point method [30,40]. The wave-mixing dipoles in Eq. (4) have a similar structure to the usual HHG dipole, however, the coefficients, $\tilde{C}_m$, are themselves complex oscillatory functions. This
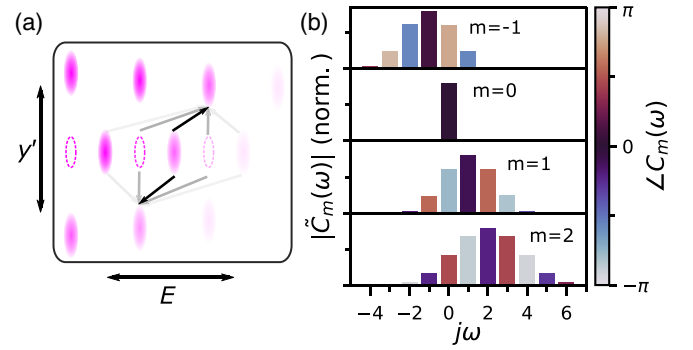

FIG. 4. (a) Illustration of the convolution picture of high-order wave mixing. The shaded ellipses in the $m = 0$ spectrum indicate the odd-order harmonics while the dashed ellipses indicate the even orders. (b) Spectrum of the wave-mixing coefficients calculated for parabolic dispersion and classical trajectories for several different pathways. The single-color birth time, t', is calculated as a function of t and $\tilde{C}_{\pm m}(j\omega)$ is calculated from the Fourier transform of Eq. (7). The color indicates the phase.

could be taken into consideration to find modified saddle-point equations [42] that yield different quantum orbits, and therefore different birth and recollision times, for each wave-mixing order. However, this procedure leads to a complicated system of equations. Instead, we treat the second harmonic field as a perturbation around the stationary points of the single-color field. We apply the saddle-point method to solve the integrals over k and t',

$$\tilde{D}_m(n\omega) = e^{im\phi}(1 - (-1)^{m+n}) \cdot$$
$$\times \int_0^{T/2} dt \, \tilde{\mathcal{D}}_0(t) \tilde{C}_m(t) e^{-in\omega t} + \text{c.c.}, \quad (5)$$

where $\tilde{\mathcal{D}}_0(t)$ is the single-color HHG dipole in the saddle-point approximation. From Fourier theory, the transform of the product, $\tilde{\mathcal{D}}_0(t)\tilde{C}_m(t)$, becomes a convolution in the frequency domain,

$$\tilde{D}_m(n\omega) = e^{im\phi}(1 - (-1)^{m+n}) \sum_{j=-\infty}^{\infty} \tilde{C}_m(j\omega)\tilde{\mathcal{D}}_0[(n-j)\omega], \quad (6)$$

where the summation is discrete because of the periodicity of the driving field. Equation (6) shows that the amplitude of each wave-mixing peak is coupled to each harmonic in the unperturbed spectrum with amplitude and phase given by $\tilde{C}_m(j\omega)$, as illustrated in Fig. 4(a). Contrary to intuition, both even and odd harmonics from the single-color spectrum contribute to each wave-mixing peak rather than those separated by 2ω. This reflects the nonperturbative and subcycle nature of the recollision physics.

To gain a deeper understanding of how the single-color HHG spectrum is mapped to the wave-mixing spectrum, in the perturbative regime the wave-mixing coefficients can be written succinctly as,

$$\tilde{C}_m(t,t') \approx \frac{(\mp 1)^{|m|} A_{2\omega}^{|m|}}{2^{|m|}|m|!} \left(\int_{t'}^{t} d\tau \, v_0 e^{\pm i2\omega\tau} \right)^{|m|}, \quad (7)$$

with the + and − signs indicating SFG and DFG pathways, respectively (Supplemental Material, IV C [35]). The sign of the complex exponential suggests that SFG (DFG) processes tend to push the spectrum upwards (downwards) in frequency. To show this more explicitly, in Fig. 4(b) we plot the wave-mixing coefficients for several orders assuming parabolic dispersion and classical trajectories. The parabolic approximation is reasonable in the present case because the cutoff of the HHG spectrum suggests that the electron-hole pairs explore only a narrow region of the Brillouin zone. As expected, the $m = 0$ coefficient is a single peak at zero frequency, so that $\tilde{D}_0(n\omega)$ is simply the single-color spectrum. The coefficients are symmetric about zero frequency for positive (negative) orders, which shows that SFG (DFG) processes push the spectrum upwards (downwards) in frequency, as expected from a photon picture of wave mixing. Thus, the asymmetry in the SFG (DFG) intensity is naturally connected to the rolloff in HHG intensity near the cutoff, as illustrated in Fig. 4(a). We note, however, that due to the complex summation in Eq. (6), the pathways of equal photon number, e.g., (8,1) and (8, −1), are inequivalent in amplitude. The perturbed trajectory picture can be used to understand other aspects of high-order wave mixing. For example, higher-order processes in $n_{2\omega}$, which have shorter trajectories, are more robust to dephasing than the single-color HHG (see Supplemental Material, I B [35]). This suggests that noncollinear HHG could be a useful tool for probing dephasing in solids, which remains a challenging problem both theoretically and experimentally [33,43,44]. Equation (7) also presents a convenient way to explore how the band structure affects the high-order wave mixing, which will be important in future experiments probing larger regions of the Brillouin zone. Finally, the assumptions of classical trajectories and fixed saddle points limits the role of the 2ω field to a phase perturbation. Amplitude modulation can be introduced into the perturbed trajectory formalism by using the complex saddle points, while Eq. (4) can be used to systematically investigate how the wave-mixing quantum orbits differ from those of the single-color field.

Conclusion. To summarize, we studied high-order XUV wave mixing in MgO using noncollinear two-color HHG. The wave-mixing intensities are determined primarily by the microscopic physics as opposed to macroscopic effects and can be understood using a perturbed-trajectory model in the strong-field approximation. We observed bright wave-mixing peaks with efficiencies that can exceed that of the single-color HHG. This suggests that, analogous to coherent control [20,45], spatially textured perturbing beams can be used to efficiently imprint petahertz currents into materials. Combined with the ability to pattern and engineer solids, this will lead to new opportunities in attosecond photonics.

[1] S. Ghimire, A. D. DiChiara, E. Sistrunk, P. Agostini, L. F. DiMauro, and D. A. Reis, Nat. Phys. **7**, 138 (2011).

[2] F. Krausz and M. I. Stockman, Nat. Photon. **8**, 205 (2014).

[3] G. Vampa, T. J. Hammond, N. Thiré, B. E. Schmidt, F. Légaré, C. R. McDonald, T. Brabec, D. D. Klug, and P. B. Corkum, Phys. Rev. Lett. **115**, 193603 (2015).

[4] Y. S. You, D. Reis, and S. Ghimire, Nat. Phys. **13**, 345 (2017).

[5] S. Jiang, S. Gholam-Mirzaei, E. Crites, J. E. Beetar, M. Singh, R. Lu, M. Chini, and C. D. Lin, J. Phys. B: At., Mol. Opt. Phys. **52**, 225601 (2019).

[6] M. R. Bionta, E. Haddad, A. Leblanc, V. Gruson, P. Lassonde, H. Ibrahim, J. Chaillou, N. Émond, M. R. Otto, A. Jiménez-Galán, R. E. F. Silva, M. Ivanov, B. J. Siwick, M. Chaker, and F. Légaré, Phys. Rev. Res. **3**, 023250 (2021).

[7] M. Hohenleutner, F. Langer, O. Schubert, M. Knorr, U. Huttner, S. W. Koch, M. Kira, and R. Huber, Nature (London) **523**, 572 (2015).

[8] A. Jiménez-Galán, R. E. F. Silva, O. Smirnova, and M. Ivanov, Nat. Photon. **14**, 728 (2020).

[9] G. Vampa, T. J. Hammond, M. Taucer, X. Ding, X. Ropagnol, T. Ozaki, S. Delprat, M. Chaker, N. Thiré, B. E. Schmidt, F. Légaré, D. D. Klug, A. Y. Naumov, D. M. Villeneuve, A. Staudte, and P. B. Corkum, Nat. Photon. **12**, 465 (2018).

[10] M. Sivis, M. Taucer, G. Vampa, K. Johnston, A. Staudte, A. Y. Naumov, D. M. Villeneuve, C. Ropers, and P. B. Corkum, Science **357**, 303 (2017).

[11] S. Cha, M. Kim, Y. Kim, S. Choi, S. Kang, H. Kim, S. Yoon, G. Moon, T. Kim, Y. W. Lee, G. Y. Cho, M. J. Park, C.-J. Kim, B. J. Kim, J. Lee, M.-H. Jo, and J. Kim, Nat. Commun. **13**, 6630 (2022).

[12] A. Korobenko, S. Rashid, C. Heide, A. Y. Naumov, D. A. Reis, P. Berini, P. B. Corkum, and G. Vampa, Phys. Rev. X **12**, 041036 (2022).

[13] G. Vampa, T. J. Hammond, N. Thiré, B. E. Schmidt, F. Légaré, C. R. McDonald, T. Brabec, and P. B. Corkum, Nature (London) **522**, 462 (2015).

[14] Y. Sanari, T. Otobe, Y. Kanemitsu, and H. Hirori, Nat. Commun. **11**, 3069 (2020).

[15] P. Jürgens, B. Liewehr, B. Kruse, C. Peltz, D. Engel, A. Husakou, T. Witting, M. Ivanov, M. J. J. Vrakking, T. Fennel, and A. Mermillod-Blondin, Nat. Phys. **16**, 1035 (2020).

[16] J. B. Bertrand, H. J. Wörner, H.-C. Bandulet, E. Bisson, M. Spanner, J.-C. Kieffer, D. M. Villeneuve, and P. B. Corkum, Phys. Rev. Lett. **106**, 023001 (2011).

[17] K. T. Kim, C. Zhang, A. D. Shiner, S. E. Kirkwood, E. Frumker, G. Gariepy, A. Naumov, D. M. Villeneuve, and P. B. Corkum, Nat. Phys. **9**, 159 (2013).

[18] D. D. Hickstein, F. J. Dollar, P. Grychtol, J. L. Ellis, R. Knut, C. Hernández-García, D. Zusin, C. Gentry, J. M. Shaw, T. Fan, K. M. Dorney, A. Becker, A. Jaroń-Becker, H. C. Kapteyn, M. M. Murnane, and C. G. Durfee, Nat. Photon. **9**, 743 (2015).

[19] Z. Li, G. Brown, D. H. Ko, F. Kong, L. Arissian, and P. B. Corkum, Phys. Rev. Lett. **118**, 033905 (2017).

[20] F. Kong, C. Zhang, F. Bouchard, Z. Li, G. G. Brown, D. H. Ko, T. J. Hammond, L. Arissian, R. W. Boyd, E. Karimi, and P. B. Corkum, Nat. Commun. **8**, 14970 (2017).

[21] C. M. heyl, P. Rudawski, F. Brizuela, S. N. Bengtsson, J. Mauritsson, and A. L'Huillier, Phys. Rev. Lett. **112**, 143902 (2014).

[22] J. L. Ellis, K. M. Dorney, C. G. Durfee, C. Hernández-García, F. Dollar, C. A. Mancuso, T. Fan, D. Zusin, C. Gentry, P. Grychtol, H. C. Kapteyn, M. M. Murnane, and D. D. Hickstein, Opt. Express **25**, 10126 (2017).

[23] M. E. Tzur, O. Neufeld, E. Bordo, A. Fleischer, and O. Cohen, Nat. Commun. **13**, 1312 (2022).

[24] G. Vampa, Y. S. You, H. Liu, S. Ghimire, and D. A. Reis, Opt. Express **26**, 12210 (2018).

[25] A. Fleischer and N. Moiseyev, Phys. Rev. A **74**, 053806 (2006).

[26] A. Fleischer, O. Kfir, T. Diskin, P. Sidorenko, and O. Cohen, Nat. Photon. **8**, 543 (2014).

[27] N. Dudovich, O. Smirnova, J. Levesque, Y. Mairesse, M. Y. Ivanov, D. M. Villeneuve, and P. B. Corkum, Nat. Phys. **2**, 781 (2006).

[28] J. Goodman, *Introduction to Fourier Optics*, 3rd ed., McGraw-Hill Physical and Quantum Electronics Series (W. H. Freeman, New York, 2005).

[29] D. Azoury, M. Krüger, G. Orenstein, H. R. Larsson, S. Bauch, B. D. Bruner, and N. Dudovich, Nat. Commun. **8**, 1453 (2017).

[30] G. Vampa, C. R. McDonald, G. Orlando, D. D. Klug, P. B. Corkum, and T. Brabec, Phys. Rev. Lett. **113**, 073901 (2014).

[31] L. Yue and M. B. Gaarde, J. Opt. Soc. Am. B **39**, 535 (2022).

[32] A. Thorpe, N. Boroumand, A. M. Parks, E. Goulielmakis, and T. Brabec, Phys. Rev. B **107**, 075135 (2023).

[33] I. Floss, C. Lemell, G. Wachter, V. Smejkal, S. A. Sato, X.-M. Tong, K. Yabana, and J. Burgdörfer, Phys. Rev. A **97**, 011401(R) (2018).

[34] R. Boyero-García, O. Zurrón-Cifuentes, L. Plaja, and C. Hernández-García, Opt. Express **29**, 2488 (2021).

[35] See Supplemental Material at http://link.aps.org/supplemental/10.1103/PhysRevA.108.L051103 for details of the semiconductor Bloch calculations and analytic model.

[36] R. E. F. Silva, F. Martín, and M. Ivanov, Phys. Rev. B **100**, 195201 (2019).

[37] J. M. Dahlström, A. L'Huillier, and J. Mauritsson, J. Phys. B: At., Mol. Opt. Phys. **44**, 095602 (2011).

[38] O. Pedatzur, G. Orenstein, V. Serbinenko, H. Soifer, B. D. Bruner, A. J. Uzan, D. S. Brambila, A. Harvey, L. Torlina, F. Morales, O. Smirnova, and N. Dudovich, Nat. Phys. **11**, 815 (2015).

[39] G. Vampa and T. Brabec, J. Phys. B: At., Mol. Opt. Phys. **50**, 083001 (2017).

[40] M. Lewenstein, P. Balcou, M. Y. Ivanov, A. L'Huillier, and P. B. Corkum, Phys. Rev. A **49**, 2117 (1994).

[41] G. Vampa, C. R. McDonald, G. Orlando, P. B. Corkum, and T. Brabec, Phys. Rev. B **91**, 064302 (2015).

[42] G. G. Brown, D. H. Ko, C. Zhang, and P. B. Corkum, Phys. Rev. A **105**, 023520 (2022).

[43] C. Heide, Y. Kobayashi, A. C. Johnson, F. Liu, T. F. Heinz, D. A. Reis, and S. Ghimire, Optica **9**, 512 (2022).

[44] J. Freudenstein, M. Borsch, M. Meierhofer, D. Afanasiev, C. P. Schmid, F. Sandner, M. Liebich, A. Girnghuber, M. Knorr, M. Kira, and R. Huber, Nature (London) **610**, 290 (2022).

[45] K. Jana, K. R. Herperger, F. Kong, Y. Mi, C. Zhang, P. B. Corkum, and S. Sederberg, Nat. Photon. **15**, 622 (2021).